

THE PIPER SURVEY: I. AN INITIAL LOOK AT THE INTRACLUSTER GLOBULAR CLUSTER POPULATION IN THE PERSEUS CLUSTER

WILLIAM E. HARRIS

Department of Physics & Astronomy
McMaster University
Hamilton ON L8S 4M1, Canada

PATRICK R. DURRELL

Department of Physics and Astronomy
Youngstown State University
Youngstown OH 44555, USA

AARON J. ROMANOWSKY

Department of Physics & Astronomy, San José State University
One Washington Square, San José CA 95192, USA

JOHN BLAKESLEE

National Research Council of Canada
Herzberg Astronomy and Astrophysics Research Centre
Victoria BC, Canada

JEAN BRODIE

University of California Observatories
1156 High Street, Santa Cruz CA 95064, USA

STEVEN JANSSENS

Department of Astronomy and Astrophysics
University of Toronto, 50 St. George St, Toronto ON M5S 3H4, Canada

THORSTEN LISKER

Astronomisches Rechen-Institut, Zentrum für Astronomie der Universität Heidelberg, Mönchhofstrae 12-14, 69120
Heidelberg, Germany

SAKURAKO OKAMOTO

Shanghai Astronomical Observatory
80 Nandan Road, Shanghai 200030, China

CAROLIN WITTMANN

Astronomisches Rechen-Institut, Zentrum für Astronomie der Universität Heidelberg, Mönchhofstrae 12-14, 69120
Heidelberg, Germany

(Dated: August 21, 2018)
to be submitted to ApJ

ABSTRACT

We describe the goals and first results of a Program for Imaging of the PERseus cluster of galaxies (PIPER). The first phase of the program builds on imaging of fields obtained with the Hubble Space Telescope ACS/WFC and WFC3/UVIS cameras. Our PIPER target fields with HST in total include major early-type galaxies including the active central giant NGC 1275; known Ultra-Diffuse Galaxies; and the Intracluster Medium. The resulting photometry, in B and I , reaches deep enough to resolve and measure the globular cluster (GC) populations in the Perseus member galaxies. Here we present initial results for three pairs of fields that confirm the presence of Intracluster GCs as distant as 740 kpc from the Perseus center, or 40% of the virial radius of the cluster. The majority of these Intracluster GCs are identifiably blue (metal-poor) but there is a trace of a red (metal-rich)

component as well, even at these very remote distances.

Keywords: galaxies: formation — galaxies: star clusters — globular clusters: general

1. INTRODUCTION

Perseus (Abell 426) at $d = 75$ Mpc offers a rich and fascinating laboratory for galaxy evolution, but it has not yet gained the level of attention that has been given, for example, to Virgo or Coma. Perseus has a velocity dispersion in the range $\sigma_v \simeq 1000 - 1300$ km s⁻¹, among the highest of clusters in the local universe (Kent & Sargent 1983; Struble & Rood 1991; Girardi et al. 1996; Weinmann et al. 2011); for comparison, the Coma cluster has $\sigma_v = 1100$ km s⁻¹ (Colless & Dunn 1996). The total mass of Perseus is almost $10^{15} M_\odot$ (Girardi et al. 1998; Simionescu et al. 2011). Enveloping the cluster is a vast halo of X-ray gas and dark matter with virial radius $r_{200} = 1.8$ Mpc (Simionescu et al. 2011), comparable to the most gas-rich and populous galaxy clusters (e.g. Zhao et al. 2013; Loewenstein 1994; Main et al. 2017).

Like Virgo and Coma, Perseus contains many large early-type galaxies, among which the most notable is the central supergiant NGC 1275 (= 3C48 = Perseus A), which sits at the center of the X-ray gas and the dynamical center of the cluster. NGC 1275 is perhaps the most extreme case in the local universe where we see the ongoing growth of a Brightest Cluster Galaxy (BCG) complete with cooling flows, feedback, and extreme star formation rate. Within NGC 1275 is a spectacular web of H α filaments extending to more than 30 kpc from galaxy center, which itself contains $\sim 10^{11} M_\odot$ of molecular gas and extended regions of star formation (e.g. Fabian et al. 2011; Matsushita et al. 2013; Canning et al. 2014).

In this paper, we describe a Program for Imaging of PERseus (called PIPER) currently underway that is intended to attack four different program goals through the use of globular cluster (GC) populations.

(1) In recent years it has become clear that rich clusters of galaxies are hosts for large numbers of Ultra-Diffuse Galaxies (UDGs), currently a focus of considerable interest (van Dokkum et al. 2015a,b; Koda et al. 2015; Martínez-Delgado et al. 2016; Román & Trujillo 2017; Papastergis et al. 2017; Amorisco et al. 2018). Perseus is already known to hold many UDG candidates (Wittmann et al. 2017), giving us the chance to improve our understanding of their demographics. Some UDGs in turn seem to have remarkably populous systems of GCs

relative to their low luminosities (Peng & Lim 2016; Beasley & Trujillo 2016; van Dokkum et al. 2016, 2018), indicating that they have massive dark halos and extremely high mass-to-light ratios (Harris et al. 2017b), while others are quite GC-poor (Lim et al. 2018; Amorisco et al. 2018). No highly consistent pattern has yet emerged, and at least some of these extreme galaxies may violate the near-constant ratio of GC system mass to halo (virial) mass obeyed by more luminous galaxies (Hudson et al. 2014; Durrell et al. 2014; Harris et al. 2017b) or simply show considerable scatter around that relation (Toloba et al. 2018; El-Badry et al. 2018; Amorisco et al. 2018).

(2) As a rich and dynamically active cluster, Perseus should also have stellar Intra-Cluster Light (ICL) built from disrupted or stripped member galaxies (e.g. Burke et al. 2012; Ramos et al. 2015; Ramos-Almendares et al. 2018). In such clusters the ICL can make up typically 10–30% of the total stellar mass. Because the ICL is actively growing particularly since $z = 1$, the sheer amount of ICL and its degree of substructure (clumpiness and tidal streams) probe the dynamical state of the entire cluster. But the stellar ICL is extremely diffuse and difficult to map out with conventional surface-brightness photometry over a field as wide as the $\sim 1^\circ$ diameter of Perseus. For such a low signal, a more effective tracer is one for which the background ‘noise’ can be reduced to near-zero levels. As will be shown below, GCs fit this bill beautifully: they are individually luminous, easy to isolate, and can be reached by *HST* for galaxies out to ~ 250 Mpc or more (Harris et al. 2016). A preliminary investigation of the GC populations in MAST Archival fields within Perseus has shown that an Intra-Cluster Globular Cluster (ICGC) population exists (Harris & Mulholland 2017, hereafter referred to as HM17) though the sheer amount of it is still quite uncertain. Substantial ICGC numbers have been detected in other large clusters including Virgo (Durrell et al. 2014), Coma (Peng et al. 2011), A1185 (West et al. 2011), and A1689 (Alamo-Martínez & Blakeslee 2017). Perhaps most importantly, multiband photometry also automatically yields their *metallicity distribution function* (MDF) since GC color is a monotonic function of [Fe/H] and is quite insensitive to age (e.g. Peng et al. 2006). The extremely faint, diffuse, integrated stellar light cannot provide this level of insight.

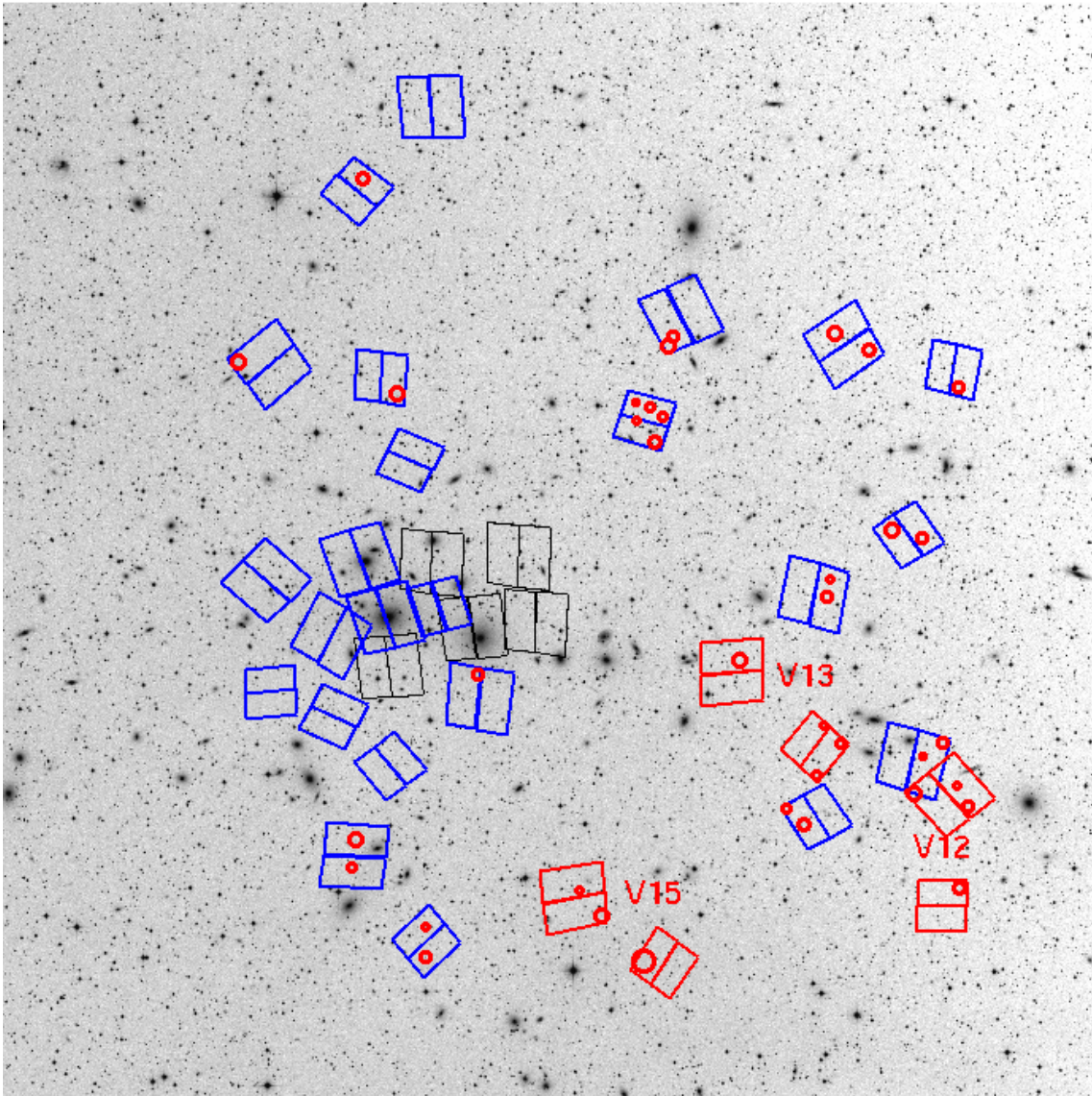


Figure 1. Image of the central region of the Perseus cluster (DSS image in blue), showing the locations of the *HST* images used in this study. North is at top, East at left and the field shown is $60' = 1300$ kpc across. NGC 1275, at the center of Perseus, is left of center. The pairs of pointings in our program are marked in blue or red (ACS are the larger squares, WFC3 the smaller squares). The five black ACS fields near the center show previous imaging from the MAST archive. The red fields and labels show the three pairs of fields discussed in the present paper (Visits 12, 13, 15). Finally, the known UDGs in Perseus that fall within our program fields are marked with the small red circles, with radii equal to $3r_{eff}$.

(3) The Perseus core has several large early-type galaxies (ETGs), particularly NGC 1275, NGC 1272, and NGC 1278. Since their projected separations are $\lesssim 100$ kpc, the total GC population in the core region will be a mutually overlapping combination of these three major galaxies, plus some smaller Perseus members, plus the ICGCs (which should follow to first order the cluster potential well). Given deep photometry with appropriate field coverage of this central region, a simultaneous solution for all these components can be performed. NGC

1275 is uniquely interesting because GC systems have never been explored in a galaxy with such extreme, high-activity conditions. If, for example, its GCS turns out to have high specific frequency (number of GCs per unit galaxy luminosity) as is the usual case for BCGs (Harris et al. 2017c), it would support the view that the current spectacular AGN and star-forming activity in its inner 20 kpc is only an add-on to a dominant early formation epoch.

(4) At the opposite end of the dwarf-galaxy structural scale from the UDGs are the Ultra-

Table 1
TARGET FIELDS

MAST Field Label	Visit	RA	Dec	R'	A_I	E_{B-I}	Target Galaxies
NGC1275-F1	V1	03:19:49.6	+41:30:36.0	0.29	0.245	0.346	NGC 1275
NGC1275-F2	V2	03:20:03.5	+41:29:39.4	3.06	0.245	0.344	Perseus core
NGC1275-F3	V3	03:19:54.5	+41:33:54.5	3.42	0.247	0.349	Perseus core
NGC1275-F4	V4	03:19:23.1	+41:26:09.3	6.53	0.242	0.341	Perseus core
NGC1275-F5	V5	03:20:23.8	+41:32:43.1	6.97	0.249	0.351	NGC 1278
PERSEUS-UDG01	V6	03:17:16.0	+41:34:10.1	28.70	0.244	0.344	WUDG 5,8,13,14
PERSEUS-UDG02	V7	03:17:00.3	+41:42:58.9	33.74	0.227	0.320	RUDG 5,6,84
PERSEUS-DUG03	V8	03:18:30.2	+41:41:07.1	17.93	0.256	0.360	WUDG 28,29,33,35,36,40,41, RUDG 25
PERSEUS-UDG04	V9	03:19:54.1	+41:54:01.7	23.35	0.276	0.388	RUDG 23,60
PERSEUS-UDG05	V10	03:19:50.2	+41:43:19.3	12.63	0.252	0.355	WUDG 83,84, RUDG 21,27
PERSEUS-UDG06	V11	03:19:39.9	+41:13:07.6	17.64	0.228	0.321	WUDG 79,80,88,89
PERSEUS-UDG07	V12	03:17:09.0	+41:14:06.4	34.11	0.227	0.319	WUDG 1,2,7, RUDG 15
PERSEUS-UDG08	V13	03:17:44.1	+41:22:51.1	24.52	0.241	0.339	WUDG 12,16,17,22
PERSEUS-UDG09	V14	03:17:45.5	+41:19:30.2	25.55	0.238	0.334	WUDG 4,6,7,18,19
PERSEUS-UDG10	V15	03:18:31.1	+41:11:31.6	24.00	0.315	0.444	WUDG 56,59, RUDG 16
PERSEUSCLUSTER1	ACS1	03:19:47.9	+41:28:00.3	2.70	0.243	0.343	NGC 1275
PERSEUSCLUSTER3	ACS3	03:19:23.2	+41:29:59.1	4.73	0.242	0.341	NGC 1272
PERSEUSCLUSTER4	ACS4	03:19:04.7	+41:30:10.9	8.15	0.243	0.342	Perseus core
PERSEUSCLUSTER5	ACS5	03:19:34.6	+41:33:37.2	3.87	0.246	0.348	Perseus core
PERSEUSCLUSTER6	ACS6	03:19:09.1	+41:33:50.4	7.95	0.246	0.346	Perseus core

NOTES: In the last column, WUDG identifiers are from Wittmann et al. (2017) while the RUDG identifiers are additional UDGs from CFHT imaging (Romanowsky et al., in progress). The last five rows list Archival fields to be used as supplementary material for the core region.

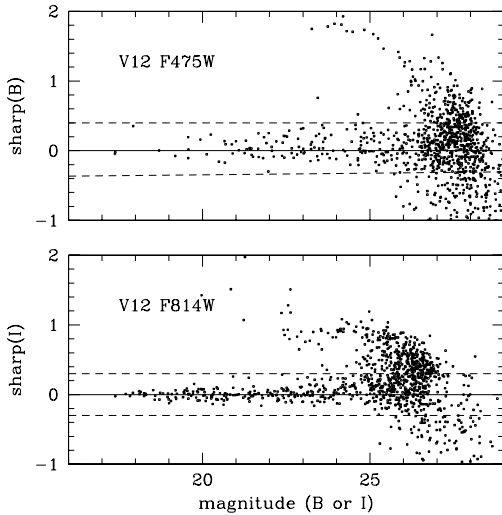


Figure 2. Illustration of the use of the *daophot* SHARP index. The example shown is for the ACS V12 field. For starlike (unresolved) objects SHARP is expected to be $\simeq 0.0$. Exclusion boundaries are drawn in as the dotted lines.

Compact Dwarfs (UCDs). Their characteristic luminosities $\gtrsim 10^7 L_\odot$ and radii $r_h \gtrsim 10$ pc distinguish them from all but the largest and most luminous GCs. These dense stellar systems may be a mixed population, either rem-

nant nuclei of stripped dwarfs, or very massive star clusters (see Mieske et al. 2012; Wittmann et al. 2016; Voggel et al. 2018, for recent discussion). At the Perseus distance, UCD candidates will be found as an automatic byproduct of our HST imaging data. From the observed scaling relation between numbers of UCDs with $M > 10^7 M_\odot$ and host cluster mass (e.g. Pfeffer et al. 2014; Janssens et al. 2017) Perseus should contain of order 200 UCDs. Some dozens of these are already known (Penny et al. 2011, 2012) and the results of our program are expected to yield enough UCDs in total to study the systematics of their spatial distributions and mean metallicities.

Lastly, we can expect to carry out an inventory of the M32-like compact ellipticals (cEs), a rare class of galaxy now also emerging as a topic of systematic study (Janz et al. 2016; Martiñočić & Micic 2017; Zhang & Bell 2017; Ferré-Mateu et al. 2018).

For the following discussion, we adopt a distance $d = 75$ Mpc for Perseus, obtained from the redshift 5207 km s^{-1} corrected to the CBR frame (NED), and a Hubble constant $H_0 = 69.7 \text{ km s}^{-1} \text{ Mpc}^{-1}$ (Hinshaw et al. 2013). From NED we also adopt mean foreground extinctions of $A_I \simeq 0.246$ and $E_{B-I} \simeq 0.346$ for an apparent distance modulus $(m - M)_I = 34.62$.

The outline of this paper is as follows: Section 2 describes the characteristics of our imaging database and the photometric measurement techniques directed towards isolating the GC candidates. Section 3 presents in turn the color-magnitude distribution of the GCs in each target field, their effective radii, their luminosity distribution, and their color distribution. Section 4 concludes with a brief summary.

2. DATABASE AND OBSERVATIONAL STRATEGY

Our new *HST* imaging data for PIPER is from Cycle 25 program 15235 (PI Harris). The ACS/WFC and WFC3/UVIS cameras are used in parallel to obtain exposures of 15 pairs of fields scattered across the cluster; these pointings are shown in Figure 1 and listed in Table 1. In the Table, successive columns list the MAST Archive field identifier; the Visit number; the field coordinates (J2000) for the Primary camera pointing in each pair; their projected distance R in arcminutes from NGC 1275 (the Perseus center); foreground extinction A_I and reddening E_{B-I} calculated from NED; and the galaxies included in each pointing.

In Table 1, for Visits 1-5, the ACS camera is the Primary and WFC3 the Parallel, while for Visits 6-15, WFC3 is the Primary and ACS the Parallel.

The core of Perseus, at center-left in the figure, is covered nearly completely out to $R \simeq 5'$ (100 kpc) when supplemented by the additional five MAST Archive ACS/WFC fields also shown in the figure. The pointings targeting the UDGs are in most cases far away from any of the major Perseus galaxies. The final five rows of Table 1 give the locations of Archival ACS fields from program 10201 (PI Conselice) that will also be used to fill in our coverage of the Perseus core regions (see also HM17). As can be seen in Table 1, the field-to-field differences in foreground reddening are modest (typically $\Delta(B - I) \lesssim 0.03$ mag) with the exception of the more heavily reddened V15.

The fields will be referred to below by their spacecraft Visit number V1–V15. The first five Visits are the ones covering the Perseus core, while the remaining 10 are the outer fields selected to cover the UDGs. Spacecraft orientations were chosen to maximize the numbers of UDGs we could capture. These 10 outlying fields will also be used to reveal ICGCs, UCDs, and any other types of dwarf-galaxy members.

The schedule of spacecraft visits is spread out over nearly a two-year period from 2017 Oct to 2019 March. At time of writing, the first three image pairs have been obtained, for V12, V13, and V15. These target three of the most remote locations from cluster center. At a scale

of 22 kpc/arcmin for a Perseus distance of 75 Mpc, V12 (for example) lies at a projected distance of 740 kpc from Perseus center (cf. Table 1), equivalent to 40% of the Perseus virial radius (Simionescu et al. 2011). In the present paper, we use the data from these three image pairs to define a consistent set of measurement procedures, and to gain an initial look at the features of the ICGC population.

For most of our program goals we need to detect and characterize GCs within Perseus, either in the target galaxies or distributed throughout the diffuse ICM. Typical GCs have half-light diameters $2r_h \simeq 5$ pc (Harris 1996, 2010 edition), which at $d = 75$ Mpc translates to $0.014''$, almost an order of magnitude smaller than the natural $0.1''$ resolution of *HST*. This means that most GCs belonging to the Perseus galaxies will be near-starlike (that is, unresolved) objects, which is a major advantage for carrying out photometry and for isolating them from the field contaminants that are dominated by faint, small background galaxies (see below). In addition, GCs fall in a relatively narrow range of color index, permitting further rejection of very blue or very red contaminants. This combination of object morphology and color gives us a very effective filtering procedure to isolate the GC population with a low level of residual contamination.

In all cases our program employs exposures in filters that maximize signal-to-noise but can also be transformed to standard (B, I) for easy comparison with previous GC data in the literature. The adopted filters are (F475W, F814W) for ACS/WFC; and (F475X, F814W) for WFC3/UVIS. Though WFC3 F475X has rarely been used, it is significantly broader than F475W and still transforms well to standard B . For Visits V6-V15, the Primary field is WFC3 with total exposure times of 2533 sec in F475X and 2653 sec in F814W. Four dithered sub-exposures are taken in each case to give a final image effectively free of cosmic rays and other artifacts. The Parallel field is ACS with total $t = 2424$ sec (F475W) and 2271 sec (F814W). In what follows, we will refer to the exposure pairs as the B and I images.

The procedure for detection and photometry of the GC candidates is similar to the steps outlined in, e.g., Harris (2009); Harris et al. (2016) or HM17. We start with the CTE-corrected, drizzled **.drc* images provided by MAST. First, both B and I exposures are registered and combined to create a master image. Source Extractor (SE) (Bertin & Arnouts 1996) is used to measure this master image and to construct a finding list, keeping only objects within the SE parameter range $1.0 \lesssim r_{1/2} \lesssim 1.5$ px (cf. Harris 2009). This first culling step eliminates obvi-

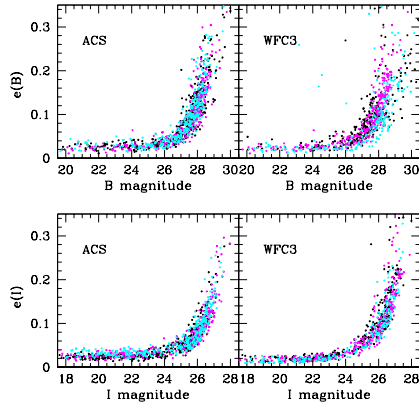


Figure 3. Photometric measurement uncertainties from *daophot/allstar* fits. Uncertainties $e(B)$ are plotted versus B (upper panels) and $e(I)$ versus I (lower panels). Data from field V12 are in black symbols, V13 in magenta, and V15 in cyan.

ous nonstellar objects, detector artifacts, and (very) occasional severely crowded objects, although crowding is not a significant problem for these extremely sparse fields.

This master finding list was then fed into *pyraf/daophot*, through the regular sequence of *phot* (through a $r = 2$ px aperture), *psf*, and *allstar*. A point-spread function (PSF) was defined empirically on each B and I image individually from a combination of typically 50 or more moderately bright, uncrowded stars. Tests were made to compare results adopting either a uniform PSF or one depending on position (x, y) in the image, but with undetectably different results. The *allstar* magnitudes were then corrected to equivalent large-aperture magnitudes. The appropriate photometric zeropoints for each filter and for the exact dates of the exposures, as taken from the STScI webpage zeropoint calculators, were then added to put the data onto the VEGAMAG system.

Final rejection of distinguishably nonstellar objects was done with the *daophot/sharp* parameter, as illustrated in Figure 2. *Sharp* is defined such that starlike objects (ones closely matching the PSF) will appear near $\simeq 0$, and exclusion regions can then be defined to reject much smaller or more extended sources as shown in the Figure. The I image has the higher SNR of the two filters for all but the bluest objects, and as expected the stellar sequence is noticeably narrower for it. Objects falling outside the *sharp* boundaries (Fig. 2) in either filter were rejected.

The cleaned measurements in each filter were matched to within $\Delta r = 2$ px in position, further rejecting any objects not appearing in both filters. The entire combination of steps described above is effective not just at culling

clearly nonstellar objects, but also spurious detections near the CCD chip edges or within the bright cores of any Perseus member galaxies falling within the fields.

The last step in the photometry was to convert the magnitudes in the native VEGAMAG filter systems (F475W, F814W for ACS, and F475X, F814W for WFC3) into B and I . For ACS these transformations are

$$B = F475W + 0.182(B - I)$$

$$I = F814W - 0.010(B - I) + 0.006(B - I)^2$$

where B is from Harris (2018, submitted) and I from Sirianni et al. (2005).

For WFC3/UVIS, we use the empirical transformations derived by Harris (2018),

$$B = F475X + 0.295$$

$$I = \begin{cases} F814W & \text{for } B - I < 1.6 \\ F814W - 0.059 + 0.037(B - I) & \text{for } B - I > 1.6. \end{cases}$$

In both cameras, F814W is very closely equal to I ; F475X is slightly redder than F475W, but the difference between them is fortunately minor (see also Deustua & Mack 2018, for a comparison of the filters between the cameras).

In Figure 3 the photometric measurement uncertainties returned by the *allstar* fits are shown versus magnitude, for the final culled list of objects.

Lastly, photometric completeness was evaluated by adding populations of artificial stars (scaled PSFs) into the images through *daophot/addstar*. The completeness ratio $f(m)$ is the number of detected stars at a given magnitude m divided by the number of artificial stars inserted at m . All of these target fields are very sparsely populated and the sky intensity level is low and quite uniform, as we illustrate

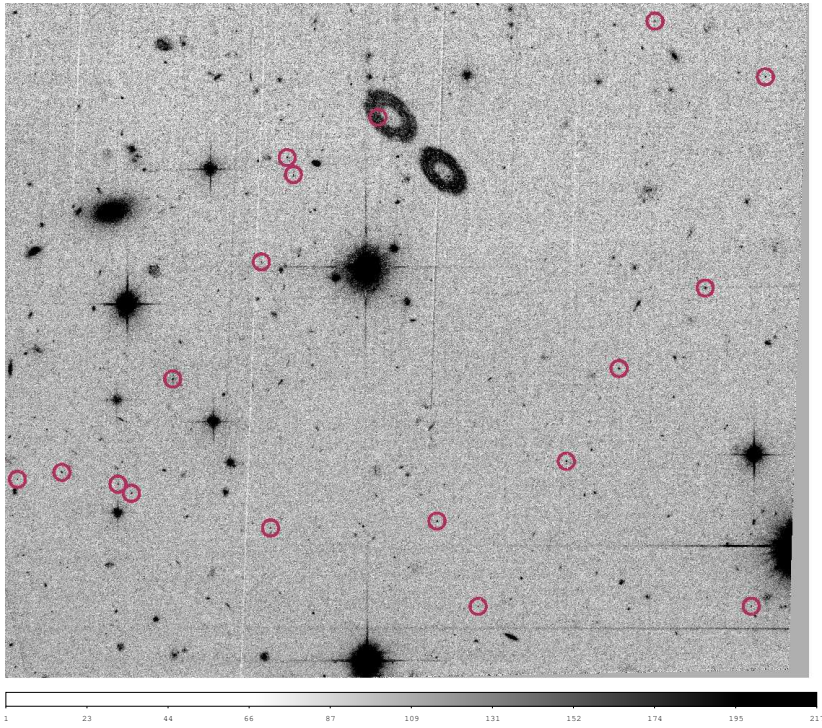


Figure 4. A section of the V15 field from the ACS camera, in F814W. The segment shown is $100''$ across. The faint objects marked with the colored circles are the GC candidates, which are starlike objects with $I < 26$ and colors in the range $1.6 < (B - I) < 2.7$.

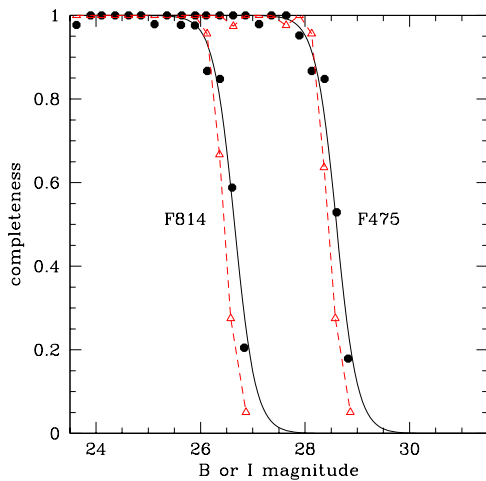


Figure 5. Photometric completeness tests for the ACS and WFC3 data. The ratio f is the fraction of starlike objects at a given B or I magnitude that were detected, plotted versus magnitude. Black points show the results for ACS and red triangles for WFC3. The completeness drops steeply from 100% to near-zero over an interval of less than a magnitude.

in Figure 4. Although many small, faint background galaxies can be seen scattered across

the frame, the numbers of similarly faint unresolved objects are quite small, and crowding is not an issue for any part of the data. Under these almost ideal circumstances, the completeness of detection will drop quite steeply from near-100% to near-zero over a short magnitude range. We model $f(m)$ with the simple two-parameter function (Harris et al. 2016)

$$f = (1 + \exp(\alpha(m - m_0)))^{-1}$$

where m_0 is the magnitude at which 50% of the objects are detected and α measures the steepness of falloff of the completeness curve. For the ACS data we find $\alpha = 5.00$ and $m_0 = 28.60(B), 26.65(I)$, while for WFC3 $\alpha = 7.00$ and $m_0 = 28.45(B), 26.50(I)$. As is also seen in Figure 5, the exposures from the two cameras are nearly matched, with ACS reaching 0.15 mag fainter.

3. RESULTS: DETECTING AND CHARACTERIZING ICGCS

Any GCs found in our (3+3) target fields will be associated either with dwarf galaxies in those fields, or the IntraCluster Medium. Decades of previous work on GC populations in other galaxies have established a remarkably consistent set of properties of GC systems, including their luminosity distributions, color (metallicity) distributions, and GC scale sizes.

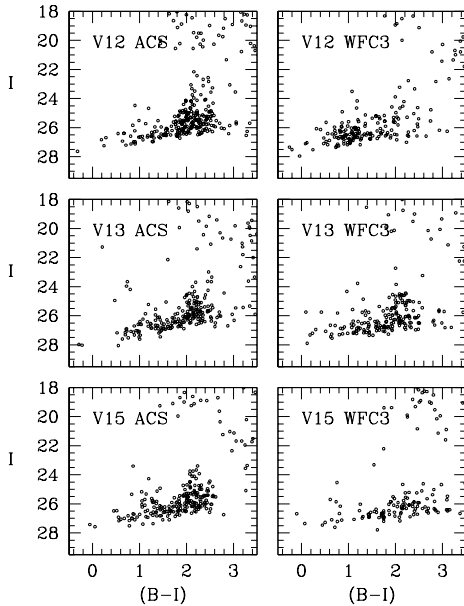


Figure 6. Color-magnitude data for starlike (unresolved) objects in the three fields. The raw measurements have been transformed to standard B, I as described in the text.

We look very briefly at each of these properties in turn, and in doing so build up the case that the Perseus GC population is clearly detected.

From analysis of a set of *HST* Archival fields (some of which are marked in Fig. 1), HM17 found evidence for the presence of ICGCs in Perseus. This preliminary finding relied on ACS and WFPC2 fields with shorter exposures than the ones in our program, and the ACS fields in particular were located in the core region near the giants NGC 1272 and 1275, making it difficult to isolate a clean sample free of contamination from Perseus galaxies. The data in our program are more optimally designed to find the intergalactic component, however much of it there is.

3.1. Color-Magnitude Data

After the image matching and rejection of nonstellar objects as described above, the resulting color-magnitude diagrams (CMDs) for our three pairs of fields are shown in Figure 6. A distinct population can be seen at intermediate color $(B - I) \simeq 2.1$ and magnitude range $I \gtrsim 23$, near the expected values for GCs. Taking into account the rapidly increasing scatter in color for $I > 26$, we isolate a “GC candidate” region defined by the box $22.5 < I < 26.0$, $1.7 < (B - I) < 2.6$. Within this box the photometry is also highly complete ($>90\%$). The boundaries of this region correspond to abso-

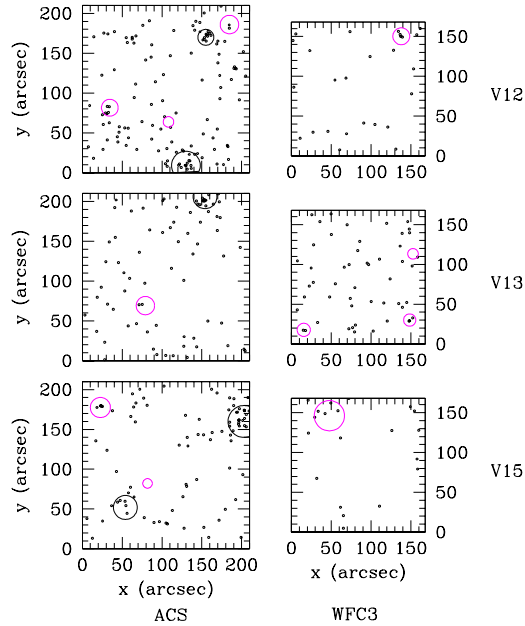


Figure 7. Locations of objects in each field that fall within the color and magnitude range for normal globular clusters ($1.6 < (B - I) < 2.7$, $22.5 < I < 26.0$). Figures on the left show the ACS camera, and on the right the WFC3 camera. Black circles indicate the positions of small galaxies that have detectable GC populations of their own; objects inside these circles are excluded from the composite CMD shown below. Magenta circles show the locations of known UDGs, where the radius of each circle is equal to $2r_{eff}$.

lute magnitudes and intrinsic colors $-12.1 < M_I < -8.6$, $1.35 < (B - I)_0 < 2.25$. For comparison, the GCs in a sample of Brightest Cluster Galaxies (Harris 2009) populate the range $M_I > -12$ and $1.4 \lesssim (B - I)_0 \lesssim 2.3$, further indicating that we are seeing a population of GCs. (Our last piece of evidence, the GC scale sizes, is presented in the next section.)

The locations (x, y) of the GC candidates on each of the fields are shown in Figure 7. Though extremely sparsely scattered across the images, nevertheless a few small concentrations of points show up, around identifiable dwarf galaxies and also some UDGs in our survey. Although there is no evidence that these dwarf-associated candidates fall in any different ranges of color or magnitude than the rest of the sample, for the purpose of isolating the ICGCs more clearly, the objects falling within the small black circles in Fig. 7 are excluded from the present analysis, though we keep ones located near the UDGs (magenta circles). The composite CMD for the dwarf-excluded sample is shown in Figure 8.

Although GC candidates are sparsely present in all six fields shown, some field-to-field varia-

tions are noticeable. Even after exclusion of the regions around the obvious dwarfs, the mean number densities seem clearly larger in some of the fields even though all are remote from the Perseus center. If the variations are not due strictly to simple stochastic differences in an already-low mean density, part of the explanation may lie in the particular locations of these fields: as can be seen in Fig. 1, V12 (ACS) and V13 (both ACS and WFC3) fall along a prominent chain of galaxies running from the Perseus core region (East side) through to IC 310 (the giant ETG on the West side, at lower right in Fig. 1) and beyond. This connection raises the possibility that ICGCs may also lie preferentially along the same axis. On a scale an order of magnitude larger, the distribution of Perseus galaxies connects with the Perseus-Pisces supercluster (Haynes & Giovanelli 1986; Wegner et al. 1993). By contrast, field V15 (ACS and WFC3) lies far off this ridgeline and there are fewer GCs. In addition, the V12 ACS field in particular falls near the giant IC 310 (at a mean separation of 90 kpc). The outskirts of the IC 310 halo may then also be contributing to the counts in V12/ACS. We will defer further discussion of these interesting possibilities until the data are in hand from our complete set of program fields.

3.2. Background Contamination

The fraction of this GC candidate sample that consists of actual Perseus GCs depends on the residual level of field contamination in the photometry – foreground stars and very faint, small background galaxies that managed to pass through the culling steps described above. Ideally we would like to assess the contamination level from a background control field near but outside Perseus. However, we have found no suitable material in the MAST archive with ACS or WFC3 filters in B , I and exposure times similar to our data. Instead, as a preliminary measure we use data from the Hubble Frontier Fields (Lotz et al. 2017). The Parallel exposures in the HFF program are with the ACS/WFC, fall on ‘blank’ fields free of any major galaxies or clusters of galaxies, and have long exposures in $F435$, $F814W$ that can be readily transformed to B , I . We have taken exposure pairs from the three HFF fields with the lowest Galactic latitudes, and measured them with exactly the same procedures as for our Perseus targets. These three HFF fields are listed in Table 2, giving the Primary target name, the coordinates of the Parallel fields, their foreground extinction, and the exposure times in B and I . (In the Table the exposure times are given for the specific image pair selected from the much longer list of HFF expo-

sure. In order to match the Perseus data better, we use these shorter-exposure pairs rather than the ultra-deep combined stacks of all exposures.) The same quantities are listed for comparison for our Perseus data.

In Figure 9, the resulting photometry for the three HFF fields combined (with total area 39 arcmin²) is shown after the same process of object selection and culling of nonstellar objects. Data from each field are corrected to the foreground reddening and extinction of Perseus. In total, just 19 objects fall clearly within the GC-candidate region defined above, and just 13 in the range $I > 24$ where most of the GC candidates lie. (Of these 13, there are 0, 8, 5 objects each from HFF fields 2, 3, 6 respectively. In the presence of small-number random variance it is unclear whether a systematic dependence on latitude is present.) Since the Perseus fields V12,13,15 cover 57.3 arcmin² in total, multiplying the HFF counts by the area ratio suggests that for $I \gtrsim 24$ field contaminants make up $\simeq 20 - 25$ objects out of the observed total of 297 objects in our GC candidate region, or a contamination fraction less than 10%.

As an additional check, we use the TRILEGAL population model of the Milky Way (Girardi et al. 2005) to estimate the numbers of foreground stars. These results are also shown in Figure 9 for a projected area on the sky of 57.3 arcmin², equal to the total area of our six program fields. The GC candidate box includes just 10 stars, again suggesting that the contamination level in our sample is small though not entirely negligible. (If the TRILEGAL counts are to be believed, this comparison also suggests that perhaps half or more of the HFF counts are from faint background galaxies small enough to pass through our selection filters.) As suggested by HM17, we conclude that sparsely spread as they are, nevertheless ICGCs are present and clearly measurable in these outlying Perseus fields, dominating over any contaminants.

3.3. Effective Radii

A bit more insight can be gained from the linear sizes of the GCs (their effective radii or diameters). Although by definition all the objects in the GC candidate list are reasonably well matched to the PSF shape, estimates of intrinsic radii can be obtained by a more detailed fit of the PSF to each object. We employ the code *ishape* (Larsen 1999) for this purpose, following many previous instances of its use in the literature for GCs in remote galaxies (e.g. Larsen 1999; Larsen et al. 2001; Georgiev et al. 2008; Harris 2009, among others).

To run *ishape* we assume an intrinsic GC profile with central concentration $c = r_t/r_c = 30$

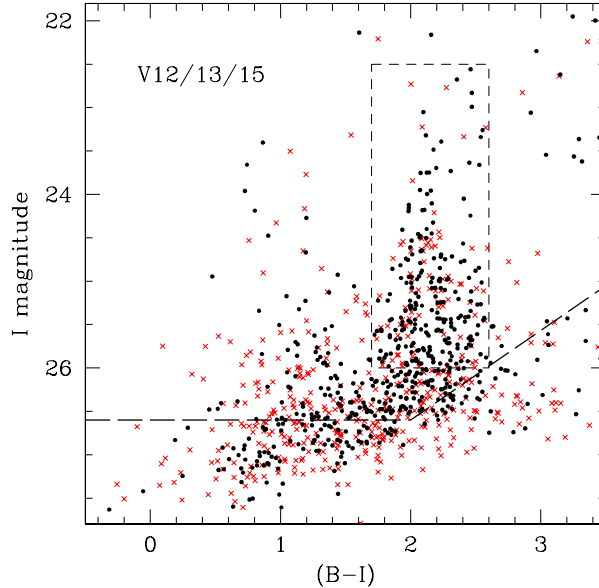


Figure 8. Composite CMD for all three visits discussed in the present paper. Black points are the three ACS images combined, red crosses are the three WFC3 images. Objects falling within any of the circles shown in the previous Figure are excluded to remove any GCs belonging to the dwarf galaxies in the fields. The 50% completeness threshold established from the completeness tests is shown as the dashed line. The box outlined in the short-dashed line marks the GC-candidate region defined in the text.

Table 2
CONTROL FIELDS

Field	Identifier	RA	Dec	ℓ	b	A_I	$t_B(\text{sec})$	$t_I(\text{sec})$
HFF2	MACSJ0416.1-2403	04:16:33.1	-24:06:48.7	327.3	+34.3	0.063	5083	5040
HFF3	MACSJ0717.5+3745	07:17:17.0	+37:49:47.3	180.5	+21.6	0.115	5044	5046
HFF6	Abell 370	02:40:13.4	-01:37:32.8	173.7	-52.9	0.046	5083	5041
Perseus		03:19:47.2	+41:30:47.0	150.6	-13.3	0.246	~ 2500	~ 2500

or $\log c = 1.5$ (KING30 in the code notation), which is an average value for GCs (Harris 1996, 2010 edition). This assumed profile is then convolved with the individual PSF for each field and matched to each object, varying the assumed $fwhm$ until a best fit is achieved. We run *ishape* only on the I -band images. The resulting SNR values returned by *ishape* and the best-fit intrinsic widths $fwhm$ for all the GC candidates are shown in Figure 10, plotted against I magnitude. The WFC3 $fwhm$ values (with $0.04''$ per px) have been multiplied by 0.8 to normalize to the ACS scale of $0.05''$ per px. The measured SNR is fairly well described by the trend

$$\log(\text{SNR}) \simeq 9.95 - 0.35I.$$

In the lower panel, the horizontal line shows $fwhm = 0.005''$ (0.1 px), below which the estimated GC sizes become extremely uncertain (cf. Larsen et al. 2001; Harris 2009). These graphs, the CMDs, and the completeness curves in Fig. 5 together show that for magnitudes $I \gtrsim 26$, the photometry and the object profiles become unreliable.

As a direct consistency test, *ishape* was also applied to the artificial stars used in the completeness tests described above; in principle, for these the fitted $fwhm$ estimates should all be zero with some stochastically generated scatter. As the lower panel of Fig. 10 shows, these artificial stars almost all lie in the range $fwhm \lesssim 0.1$ px = $0.005''$, which is equivalent to a lin-

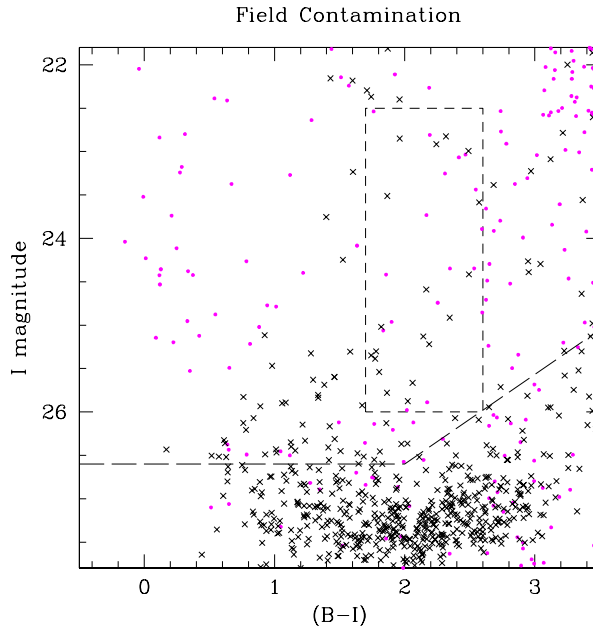


Figure 9. CMD for expected field contamination. Black crosses are from the three Hubble Frontier Fields described in the text, while magenta dots are a sample of the predicted population of Milky Way foreground stars from the TRILEGAL model. The box marked out by the dashed line indicates the GC-candidate region for Perseus; compare with Figure 8. The 50% photometric completeness limit is marked out by the long-dashed line.

ear size of $\simeq 2$ pc. This level is a reasonable indicator of the resolution limit for the profile fits.

In Figure 11 the same data are displayed in histogram form, now converted to half-light radii in parsec units. For a standard KING30 model, $r_h = 1.48 fwhm$. Only the high-quality GC candidates as defined above, with $22.5 < I < 26$ and with $1.7 < (B - I) < 2.6$, are included here. The distribution of Perseus GCs is clearly more extended than the (shaded) histogram for completely unresolved objects (i.e. simulated stars). For comparison the r_h distribution is shown for Milky Way clusters (Harris 1996, 2010 edition). To the extent allowed by the resolution limits of our imaging and the small sample sizes, the histograms for the Milky Way and Perseus GCs agree quite well.

3.4. Luminosity Function

Old GC populations consistently follow a Gaussian-like luminosity function (LF) in number per unit magnitude (e.g. Jordán et al. 2007; Villegas et al. 2010; Harris et al. 2014), so an additional test of the nature of the Perseus candidates is the shape of their LF. This is shown in Figure 12 for the combined candidate sample. At present, only a very rough test can be made again because of sample size. The pre-

vious work of HM17 shows similar results with a much bigger statistical sample, though their data include a higher fraction of GCs from the Perseus core galaxies.

The turnover (peak) absolute magnitude of the GCLF, and its dispersion σ have typical values $M_I^0 \simeq -8.3$ and $\sigma \simeq 1.3$ for large galaxies. However, both the turnover and dispersion depend systematically on host galaxy luminosity (cf. Villegas et al. 2010) such that larger galaxies have progressively more luminous turnovers (at the rate of $\simeq 0.04$ mag per galaxy absolute magnitude) and broader GCLFs (at the rate of $\simeq 0.1$ mag per galaxy absolute magnitude). Recent modelling indicates that the biggest contributions to the ICL are stars stripped from dwarf-sized to intermediate-sized galaxies (Harris et al. 2017a; Ramos-Almendares et al. 2018). Such galaxies are 3 mag or more fainter than the giants that much of the previous GCLF literature has concentrated on. Thus in principle, accurate determination of the GCLF parameters for the ICGC component would provide an additional observational test of its origin. With this in mind, we may expect very roughly $\sigma \sim 1.0$ and $M_I^0 \sim -8.2$ or a turnover apparent magnitude $I^0 \simeq 26.4$, almost half a magnitude fainter than the limit of our GC candidate data. Under these circumstances, both

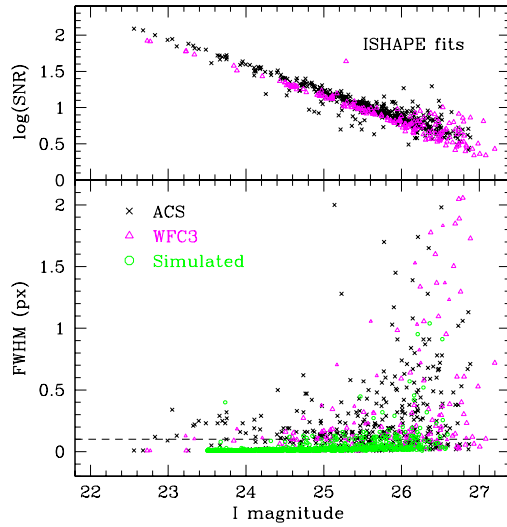


Figure 10. Results of ISHAPE measurement tests. *Upper panel:* Signal-to-noise ratio returned by *ishape*. Data from ACS are in black, WFC3 in magenta. *Lower panel:* The fwhm returned by the ISHAPE fits is plotted versus I magnitude. Simulated stars from *daophot/addstar* are green open circles. The WFC3 values have been multiplied by $0.04''/0.05'' = 0.8$ to normalize to the ACS image scale of $0.05''/\text{px}$. The dashed line at $\text{fwhm} = 0.1 \text{ px}$ shows a threshold below which objects are difficult to resolve unambiguously, as described in the text.

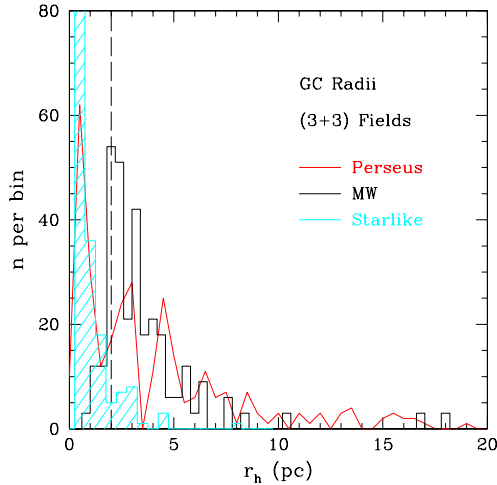


Figure 11. Histogram of intrinsic half-light radius (r_h or r_{eff}) as deduced from the ISHAPE fitting; r_h is now shown in parsec units. The Perseus objects in the GC candidate list are shown as the red solid line; simulated starlike objects in the same magnitude range as the cyan shaded histogram; and Milky Way GCs as the dashed histogram. The vertical dashed line at $r_h \simeq 2 \text{ pc}$ indicates the effective resolution limit (see text).

I^0 and σ cannot be solved simultaneously very accurately (e.g. Hanes & Whittaker 1987), so instead we simply assume different I^0 values in the range $26.0 - 26.4$ and solve for σ as a consistency test of the Gaussian form. Least-squares fits yield $\sigma = (1.23, 1.18, 1.35) \pm 0.06$ for $I^0 = (26.0, 26.2, 26.4)$. Given the small sample and perhaps some effect from residual field contamination, these fits are consistent with the

basic assumption of the standard LF shape.

3.5. Color Distribution: Blue and Red Fractions

In most luminous galaxies the color-index distribution function (CDF) for GCs is roughly bimodal, with “blue” and “red” sequences separated by ~ 1 dex in metallicity $[\text{Fe}/\text{H}]$ (e.g. Larsen et al. 2001; Brodie & Strader 2006; Peng

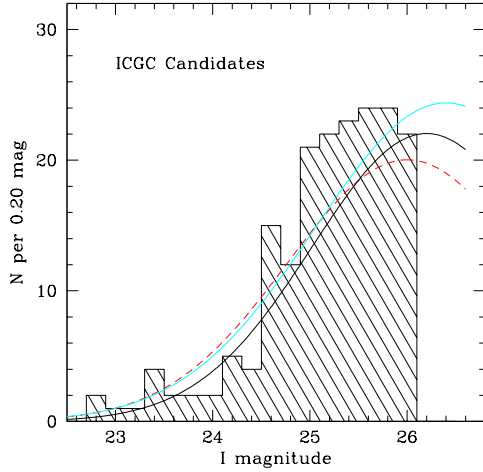


Figure 12. Luminosity distribution of the GC candidates plotted as number per unit I magnitude. Gaussian curves are shown for $(I^0, \sigma) = (6.0, 1.23)$ (dashed red line), $(26.2, 1.18)$ (solid black line), and $(26.4, 1.35)$ (cyan line).

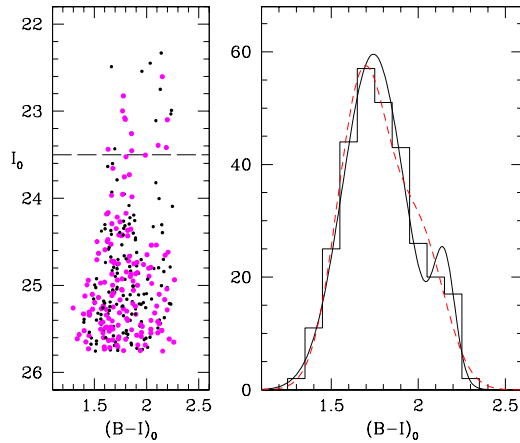


Figure 13. *Left panel:* CM diagram for all GC candidates with measured *ishape* parameters as described in the text, including both ACS and WFC3 data. Here each of the three fields is individually dereddened with the A_I, E_{B-I} values given in Table 1. Candidates with $r_h > 2$ pc are shown as larger magenta points, smaller ones as small black points. The bright-end cutoff at $I_0 = 23.5$ is shown as the dashed line. *Right panel:* Distribution in $(B - I)_0$ for the GC candidates, including data from both ACS and WFC3 and in the magnitude range $23.5 < I_0 < 26.0$. Gaussian fits to the color distribution are shown as the solid line (heteroscedastic) and dashed red line (homoscedastic).

et al. 2006; Harris 2009; Harris et al. 2017c). This is not a universal phenomenon, however,

and for the most luminous giants in particular, the CDF becomes more uniformly populated with a more continuous range in metallicities (Harris et al. 2016, 2017c). Models for the generation of the ICL and ICGCs (cf. the references cited above) further demonstrate that the higher-metallicity GCs should follow a spatial distribution more centrally concentrated to the cluster core, like the member galaxies, whereas the low-metallicity GCs stripped primarily from the dwarfs and outer halos of the member galaxies should follow a more extended distribution closer to the dark-matter potential well. The ICGC data from across the Virgo cluster (Durrell et al. 2014) and the inner part of Coma (Peng et al. 2011) are consistent with this prediction.

In HM17, $(V - I)$ photometry from five ACS fields and six WFC2 fields was used for a preliminary assessment of the ICGC. In four of the ACS fields the GC population is dominated by the giant central galaxies, but the fifth located $R \simeq 180$ kpc from cluster center may have a significant ICGC component. The CDF there is predominantly blue (blue fraction $f_b = 0.64 \pm 0.11$) along with tentative evidence for a smaller red component and thus bimodality. The more remote WFC2 fields, located 250 – 450 kpc from the center, are free of major galaxies but their limiting magnitudes are too bright to permit accurate assessment of the CDF. Nevertheless, for these more remote fields the blue GC fraction was found to be $f_b = 0.90 \pm 0.07$. The limited evidence from these fields is thus consistent with increasing dominance of the blue metal-poor component with increasing distance from cluster center.

The three pairs of fields from V12/13/15 are even more remote and the photometry is deep enough to estimate blue/red fractions. In Figure 13 (left panel) the CMD is shown for all the GC candidates with measured radii from *ishape*. The data are now dereddened with the A_I, E_{B-I} values for each individual field as listed in Table 1. In the CMD, there is no apparent difference in the distributions for the candidates that are marginally resolved ($r_h > 2$ pc, as discussed above) or unresolved ($r_h < 2$ pc). We therefore use all the candidates to construct the CDF.

The GMM (Gaussian Mixture Model) code (Muratov & Gnedin 2010) is used to carry out bimodal Gaussian fits to the CDF, with the results as shown in the right panel of Fig. 13. Here, we exclude only the data near the brighter dwarf galaxies (black circles in Fig. 7) but do not make any attempt at present to account for the UDGs in the fields. We also exclude objects with $I_0 < 23.5$ (see left panel of Fig. 13) to avoid confusion with possible UCDs.

With just $n = 298$ remaining datapoints a full heteroscedastic fit (unequal variances) is a bit risky, but making the assumption of unequal variances we obtain a mean and standard deviation $\mu_1 = 1.743 \pm 0.017$, $\sigma_1 = 0.178 \pm 0.011$ for the blue component and $\mu_2 = 2.149 \pm 0.027$, $\sigma_2 = 0.062 \pm 0.015$ for the red component, with the blue GCs making up a fraction $f_b = 0.892 \pm 0.043$ of the total. These results are similar to the WFPC2 fields from HM17. Since $\Delta(B-I)/\Delta[\text{Fe}/\text{H}] = 0.39$ (Barmby et al. 2000; Harris et al. 2006), the color difference $(\mu_2 - \mu_1) = 0.406 \pm 0.032$ between the red and blue modes corresponds to a metallicity difference $\Delta[\text{Fe}/\text{H}] \simeq 1.0$ dex, a normal value found in most galaxies.

If we simplify the solution to a homoscedastic (equal variances) case, we obtain $\mu_1 = 1.682$, $\mu_2 = 2.007$ with $\sigma_1 = \sigma_2 = 0.146$ and $f_b = 0.68$. Requiring equal σ 's has the effect of increasing the red-mode variance and drawing it in to somewhat bluer color in order to match the CDF. Both of the solutions are shown in Fig. 13. There is little to choose between them, but in both cases a unimodal CDF is rejected with $> 99\%$ confidence. At present, we conclude only that the ICGCs in these quite remote fields show a CDF consistent with a relatively normal bimodal distribution; it is dominated by the metal-poor component but a small metal-richer component appears to be present as well. More definite conclusions will have to await samples from the other fields in our survey.

4. SUMMARY

We describe the outline of our imaging program (PIPER) for the giant Perseus cluster of galaxies, with the *HST* ACS and WFC3 cameras. Exposures are designed to be deep enough to reach almost to the LF turnover point of the globular cluster systems in the Perseus galaxies. Upon completion, the program will include photometry in 35 different ACS or WFC3 fields extending from the cluster center (NGC 1275) out to projected radial distances more than 700 kpc from center. The main goals for this program are to survey the globular cluster populations around the giant galaxies in the Perseus core, in 40 UDG candidates, and in the Intra-Cluster Medium, in addition to building a more

comprehensive sample of the UCDs and cEs in Perseus.

Data from the first three pointings of the program are presented here, along with an outline of the photometric reduction methods used to rigorously isolate GCs down to an effective limiting magnitude $I = 26$ ($M_I = -8.6$). These first results show that even at distances $R > 700$ kpc, a sparse intergalactic population of GCs is clearly detectable, and even dominant over sources of field contamination. These ICGCs have magnitudes, color indices, linear sizes, and a luminosity distribution that comfortably match conventional GCs in nearby galaxies. Stronger conclusions about all these properties await the completion of the observational program. Once all the fields are in hand, an exciting prospect will be to gauge the spatial distribution of the ICGC and the radial change in its metallicity distribution, leading to a stronger link with models for the origin of the ICL.

In future papers of this series, analyses will concentrate on the UDGs and their own GC populations, the central giant galaxies, and the UCDs and compact ellipticals to be discovered in our target fields.

WEH acknowledges financial support from NSERC (Natural Sciences and Engineering Research Council of Canada). AJR was supported by National Science Foundation grant AST-1515084 and as a Research Corporation for Science Advancement Cottrell Scholar. AJR and PRD are supported by funds provided by NASA through grant GO-15235 from the Space Telescope Science Institute, which is operated by the Association of Universities for Research in Astronomy, Incorporated, under NASA contract NAS5-26555. CW and TL are supported by the Deutsche Forschungsgemeinschaft (DFG, German Research Foundation) through project 394551440. TL acknowledges financial support from the European Union's Horizon 2020 research and innovation programme under the Marie Skłodowska-Curie grant agreement No. 721463 to the SUNDIAL ITN network.

HST (ACS, WFC3)

REFERENCES

- Alamo-Martínez, K. A. & Blakeslee, J. P. 2017, ApJ, 849, 6
 Amorisco, N. C., Monachesi, A., Agnello, A., & White, S. D. M. 2018, MNRAS, 475, 4235
 Barmby, P., Huchra, J. P., Brodie, J. P., Forbes, D. A., Schroder, L. L., & Grillmair, C. J. 2000, AJ, 119, 727
 Beasley, M. A. & Trujillo, I. 2016, ApJ, 830, 23
 Bertin, E. & Arnouts, S. 1996, A&AS, 117, 393
 Brodie, J. P. & Strader, J. 2006, ARA&A, 44, 193
 Burke, C., Collins, C. A., Stott, J. P., & Hilton, M. 2012, MNRAS, 425, 2058

- Canning, R. E. A., Ryon, J. E., Gallagher, J. S., Kotulla, R., O'Connell, R. W., Fabian, A. C., Johnstone, R. M., Conselice, C. J., Hicks, A., Rosario, D., & Wyse, R. F. G. 2014, *MNRAS*, 444, 336
- Colless, M. & Dunn, A. M. 1996, *ApJ*, 458, 435
- Deustua, S. E. & Mack, J. 2018, Comparing the ACS/WFC and WFC3/UVIS Calibration and Photometry, Tech. rep.
- Durrell, P. R., Côté, P., Peng, E. W., Blakeslee, J. P., Ferrarese, L., Mihos, J. C., Puzia, T. H., Lançon, A., Liu, C., Zhang, H., Cuillandre, J.-C., McConnachie, A., Jordán, A., Accetta, K., Boissier, S., Boselli, A., Courteau, S., Duc, P.-A., Emsellem, E., Gwyn, S., Mei, S., & Taylor, J. E. 2014, *ApJ*, 794, 103
- El-Badry, K., Quataert, E., Weisz, D. R., Choksi, N., & Boylan-Kolchin, M. 2018, *ArXiv e-prints*
- Fabian, A. C., Sanders, J. S., Allen, S. W., Canning, R. E. A., Churazov, E., Crawford, C. S., Forman, W., Gabany, J., Hlavacek-Larrondo, J., Johnstone, R. M., Russell, H. R., Reynolds, C. S., Salomé, P., Taylor, G. B., & Young, A. J. 2011, *MNRAS*, 418, 2154
- Ferré-Mateu, A., Forbes, D. A., Romanowsky, A. J., Janz, J., & Dixon, C. 2018, *MNRAS*, 473, 1819
- Georgiev, I. Y., Goudfrooij, P., Puzia, T. H., & Hilker, M. 2008, *AJ*, 135, 1858
- Girardi, L., Groenewegen, M. A. T., Hatziminaoglou, E., & da Costa, L. 2005, *A&A*, 436, 895
- Girardi, M., Fadda, D., Giuricin, G., Mardirossian, F., Mezzetti, M., & Biviano, A. 1996, *ApJ*, 457, 61
- Girardi, M., Giuricin, G., Mardirossian, F., Mezzetti, M., & Boschin, W. 1998, *ApJ*, 505, 74
- Hanes, D. A. & Whittaker, D. G. 1987, *AJ*, 94, 906
- Harris, K. A., Debattista, V. P., Governato, F., Thompson, B. B., Clarke, A. J., Quinn, T., Willman, B., Benson, A., Farrah, D., Peng, E. W., Elliott, R., & Petty, S. 2017a, *MNRAS*, 467, 4501
- Harris, W. E. 1996, *AJ*, 112, 1487
- . 2009, *ApJ*, 699, 254
- Harris, W. E., Blakeslee, J. P., & Harris, G. L. H. 2017b, *ApJ*, 836, 67
- Harris, W. E., Blakeslee, J. P., Whitmore, B. C., Gnedin, O. Y., Geisler, D., & Rothberg, B. 2016, *ApJ*, 817, 58
- Harris, W. E., Ciccone, S. M., Eadie, G. M., Gnedin, O. Y., Geisler, D., Rothberg, B., & Bailin, J. 2017c, *ApJ*, 835, 101
- Harris, W. E., Morningstar, W., Gnedin, O. Y., O'Halloran, H., Blakeslee, J. P., Whitmore, B. C., Côté, P., Geisler, D., Peng, E. W., Bailin, J., Rothberg, B., Cockcroft, R., & Barber DeGraaff, R. 2014, *ApJ*, 797, 128
- Harris, W. E. & Mulholland, C. J. 2017, *ApJ*, 839, 102
- Harris, W. E., Whitmore, B. C., Karakla, D., Okoń, W., Baum, W. A., Hanes, D. A., & Kavelaars, J. J. 2006, *ApJ*, 636, 90
- Haynes, M. P. & Giovanelli, R. 1986, *ApJ*, 306, L55
- Hinshaw, G., Larson, D., Komatsu, E., Spergel, D. N., Bennett, C. L., Dunkley, J., Nolte, M. R., Halpern, M., Hill, R. S., Odegard, N., Page, L., Smith, K. M., Weiland, J. L., Gold, B., Jarosik, N., Kogut, A., Limon, M., Meyer, S. S., Tucker, G. S., Wollack, E., & Wright, E. L. 2013, *ApJS*, 208, 19
- Hudson, M. J., Harris, G. L., & Harris, W. E. 2014, *ApJ*, 787, L5
- Janssens, S., Abraham, R., Brodie, J., Forbes, D., Romanowsky, A. J., & van Dokkum, P. 2017, *ApJ*, 839, L17
- Janz, J., Norris, M. A., Forbes, D. A., Huxor, A., Romanowsky, A. J., Frank, M. J., Escudero, C. G., Faifer, F. R., Forte, J. C., Kannappan, S. J., Maraston, C., Brodie, J. P., Strader, J., & Thompson, B. R. 2016, *MNRAS*, 456, 617
- Jordán, A., McLaughlin, D. E., Côté, P., Ferrarese, L., Peng, E. W., Mei, S., Villegas, D., Merritt, D., Tonry, J. L., & West, M. J. 2007, *ApJS*, 171, 101
- Kent, S. M. & Sargent, W. L. W. 1983, *AJ*, 88, 697
- Koda, J., Yagi, M., Yamanoi, H., & Komiyama, Y. 2015, *ApJ*, 807, L2
- Larsen, S. S. 1999, *A&AS*, 139, 393
- Larsen, S. S., Brodie, J. P., Huchra, J. P., Forbes, D. A., & Grillmair, C. J. 2001, *AJ*, 121, 2974
- Lim, S., Peng, E. W., Cote, P., Sales, L. V., den Brok, M., Blakeslee, J. P., & Guhathakurta, P. 2018, *ArXiv e-prints*
- Loewenstein, M. 1994, *ApJ*, 431, 91
- Lotz, J. M., Koekemoer, A., Coe, D., Grogin, N., Capak, P., Mack, J., Anderson, J., Avila, R., Barker, E. A., Borncamp, D., Brammer, G., Durbin, M., Gunning, H., Hilbert, B., Jenkner, H., Khandrika, H., Levay, Z., Lucas, R. A., MacKenty, J., Ogaz, S., Porterfield, B., Reid, N., Robberto, M., Royle, P., Smith, L. J., Storrie-Lombardi, L. J., Sunnquist, B., Surace, J., Taylor, D. C., Williams, R., Bullock, J., Dickinson, M., Finkelstein, S., Natarajan, P., Richard, J., Robertson, B., Tumlinson, J., Zitrin, A., Flanagan, K., Sembach, K., Soifer, B. T., & Mountain, M. 2017, *ApJ*, 837, 97
- Main, R. A., McNamara, B. R., Nulsen, P. E. J., Russell, H. R., & Vantyghem, A. N. 2017, *MNRAS*, 464, 4360
- Martínez-Delgado, D., Läscher, R., Sharina, M., Toloba, E., Fliri, J., Beaton, R., Valls-Gabaud, D., Karachentsev, I. D., Chonis, T. S., Grebel, E. K., Forbes, D. A., Romanowsky, A. J., Gallego-Labordá, J., Teuwen, K., Gómez-Flechoso, M. A., Wang, J., Guhathakurta, P., Kaisin, S., & Ho, N. 2016, *AJ*, 151, 96
- Martinović, N. & Micic, M. 2017, *MNRAS*, 470, 4015
- Matsushita, K., Sakuma, E., Sasaki, T., Sato, K., & Simionescu, A. 2013, *ApJ*, 764, 147
- Mieske, S., Hilker, M., & Mergeld, I. 2012, *A&A*, 537, A3
- Muratov, A. L. & Gnedin, O. Y. 2010, *ApJ*, 718, 1266
- Papastergis, E., Adams, E. A. K., & Romanowsky, A. J. 2017, *A&A*, 601, L10
- Peng, E. W., Ferguson, H. C., Goudfrooij, P., Hammer, D., Lucey, J. R., Marzke, R. O., Puzia, T. H., Carter, D., Balcells, M., Bridges, T., Chiboucas, K., del Burgo, C., Graham, A. W., Guzmán, R., Hudson, M. J., Matković, A., Merritt, D., Miller, B. W., Mouhcine, M., Phillipps, S., Sharples, R., Smith, R. J., Tully, B., & Verdoes Kleijn, G. 2011, *ApJ*, 730, 23
- Peng, E. W., Jordán, A., Côté, P., Blakeslee, J. P., Ferrarese, L., Mei, S., West, M. J., Merritt, D., Milosavljević, M., & Tonry, J. L. 2006, *ApJ*, 639, 95
- Peng, E. W. & Lim, S. 2016, *ApJ*, 822, L31
- Penny, S. J., Conselice, C. J., de Rijcke, S., Held, E. V., Gallagher, J. S., & O'Connell, R. W. 2011, *MNRAS*, 410, 1076
- Penny, S. J., Forbes, D. A., & Conselice, C. J. 2012, *MNRAS*, 422, 885
- Pfeffer, J., Griffen, B. F., Baumgardt, H., & Hilker, M. 2014, *MNRAS*, 444, 3670
- Ramos, F., Coenda, V., Muriel, H., & Abadi, M. 2015, *ApJ*, 806, 242
- Ramos-Almendares, F., Abadi, M., Muriel, H., & Coenda, V. 2018, *ApJ*, 853, 91
- Román, J. & Trujillo, I. 2017, *MNRAS*, 468, 4039

- Simionescu, A., Allen, S. W., Mantz, A., Werner, N., Takei, Y., Morris, R. G., Fabian, A. C., Sanders, J. S., Nulsen, P. E. J., George, M. R., & Taylor, G. B. 2011, *Science*, 331, 1576
- Sirianni, M., Jee, M. J., Benítez, N., Blakeslee, J. P., Martel, A. R., Meurer, G., Clampin, M., De Marchi, G., Ford, H. C., Gilliland, R., Hartig, G. F., Illingworth, G. D., Mack, J., & McCann, W. J. 2005, *PASP*, 117, 1049
- Struble, M. F. & Rood, H. J. 1991, *ApJS*, 77, 363
- Toloba, E., Lim, S., Peng, E., Sales, L. V., Guhathakurta, P., Mihos, J. C., Côté, P., Boselli, A., Cuillandre, J.-C., Ferrarese, L., Gwyn, S., Lançon, A., Muñoz, R., & Puzia, T. 2018, *ApJ*, 856, L31
- van Dokkum, P., Abraham, R., Brodie, J., Conroy, C., Danieli, S., Merritt, A., Mowla, L., Romanowsky, A., & Zhang, J. 2016, *ApJ*, 828, L6
- van Dokkum, P., Cohen, Y., Danieli, S., Kruijssen, J. M. D., Romanowsky, A. J., Merritt, A., Abraham, R., Brodie, J., Conroy, C., Lokhorst, D., Mowla, L., O’Sullivan, E., & Zhang, J. 2018, *ApJ*, 856, L30
- van Dokkum, P. G., Abraham, R., Merritt, A., Zhang, J., Geha, M., & Conroy, C. 2015a, *ApJ*, 798, L45
- van Dokkum, P. G., Romanowsky, A. J., Abraham, R., Brodie, J. P., Conroy, C., Geha, M., Merritt, A., Villaume, A., & Zhang, J. 2015b, *ApJ*, 804, L26
- Villegas, D., Jordán, A., Peng, E. W., Blakeslee, J. P., Côté, P., Ferrarese, L., Kissler-Patig, M., Mei, S., Infante, L., Tonry, J. L., & West, M. J. 2010, *ApJ*, 717, 603
- Voggel, K. T., Seth, A. C., Neumayer, N., Mieske, S., Chilingarian, I., Ahn, C., Baumgardt, H., Hilker, M., Nguyen, D. D., Romanowsky, A. J., Walsh, J. L., den Brok, M., & Strader, J. 2018, *ApJ*, 858, 20
- Wegner, G., Haynes, M. P., & Giovanelli, R. 1993, *AJ*, 105, 1251
- Weinmann, S. M., Lisker, T., Guo, Q., Meyer, H. T., & Janz, J. 2011, *MNRAS*, 416, 1197
- West, M. J., Jordán, A., Blakeslee, J. P., Côté, P., Gregg, M. D., Takamiya, M., & Marzke, R. O. 2011, *A&A*, 528, A115
- Wittmann, C., Lisker, T., Ambachew Tilahun, L., Grebel, E. K., Conselice, C. J., Penny, S., Janz, J., Gallagher, J. S., Kotulla, R., & McCormac, J. 2017, *MNRAS*, 470, 1512
- Wittmann, C., Lisker, T., Pasquali, A., Hilker, M., & Grebel, E. K. 2016, *MNRAS*, 459, 4450
- Zhang, Y. & Bell, E. F. 2017, *ApJ*, 835, L2
- Zhao, H.-H., Jia, S.-M., Chen, Y., Li, C.-K., Song, L.-M., & Xie, F. 2013, *ApJ*, 778, 124